

Document downloaded from:

<http://hdl.handle.net/10251/153684>

This paper must be cited as:

Afonso, CRM.; Vidilli, AL.; Spinelli, JE.; Riva, R.; Amigó, V.; Kiminami, CS. (2017). An assessment of microstructure and properties of laser clad coatings of ultrafine eutectic beta Ti-Fe-Nb-Sn composite for implants. *Surface and Coatings Technology*. 328:161-171. <https://doi.org/10.1016/j.surfcoat.2017.08.035>



The final publication is available at

<https://doi.org/10.1016/j.surfcoat.2017.08.035>

Copyright Elsevier

Additional Information

An assessment of microstructure and properties of laser clad coatings of ultrafine eutectic β Ti-Fe-Nb-Sn composite for implants

C.R.M. Afonso¹, A. L. Vidilli¹, J. E. Spinelli^{1,*}, R. Riva²,
V. Amigó³ and C. S. Kiminami¹

¹ Department of Materials Engineering (DEMa), Federal University of São Carlos (UFSCar), CEP 13565-905 São Carlos, SP, Brazil.

²Institute for Advanced Studies (IEAv), Department of Aerospace Science and Technology (DCTA), PO Box 6044, 12228-970, São José dos Campos, SP, Brazil.

³ Institute of Materials Technology (ITM), Universitat Politècnica de València (UPV), P.O.Box 22012, E-46071, Valencia, Spain.

Abstract

Ultrafine eutectic Ti-based nanocomposite alloys exhibit high mechanical strength (1,800-2,500 MPa), elastic modulus nearest human bone (50-110 GPa) and good corrosion resistance due to a combination of soft β -Ti (bcc) matrix and hard/refined TiFe and/or Ti₃Sn intermetallic particles. The present study focuses on the production and characterization of Ti-Fe-Nb-Sn eutectic alloys using biocompatible β -stabilizer elements, such as Nb, Fe and Sn. Different fabrication techniques based on rapid solidification and with further evaluation of the generated properties may be highlighted considering the application of these alloys as implant material. In the present investigation, the proposed processing routes comprise single tracks and coatings (overlapped tracks) by laser melting of pre-alloyed powders of the Ti₆₆Fe₂₀Nb₈Sn₆ alloy deposited into a Ti substrate. To select this composition, three Ti-Fe-Nb based compositions of interest were originally generated under bulk conditions by using a suction casting apparatus and were further evaluated. All samples were analyzed by metallography, X-ray diffraction (XRD), scanning electron microscopy (SEM-EBSD and SEM-EDS), microhardness, nanohardness and elastic modulus. The results showed that the proportions of the formed TiFe and Ti₃Sn intermetallic particles dispersed within the soft β -Ti matrix play a fundamental role on the final properties. Lower elastic modulus ($E \sim 72$ GPa) is associated with the Ti₆₆Fe₂₀Nb₈Sn₆ bulk alloy, whereas laser clad coatings for the Ti₆₆Fe₂₀Nb₈Sn₆ alloy showed a broad range of nanohardness (4.8 - 8.0 GPa) and elastic modulus (98 - 150 GPa) depending on the related laser power and scanning speeds.

Keywords: Ti-Fe base alloy, rapid solidification, laser cladding, ultrafine eutectic, implant coatings.

* Corresponding author → E-mail address: spinelli@ufscar.br

1. Introduction

A synthesis of new Ti-based ultrafine composites and bulk metallic glasses (BMG) alloys was carried out due to their good engineering properties. These alloys are industrially important as structural and functional materials [1-5]. Ti-based BMG alloys exhibit high strength (1800–2500 MPa), low elastic modulus (50–110 GPa) and, as expected, good corrosion resistance in various solutions. For instance, $\text{Ti}_{45}\text{Zr}_{10}\text{Pd}_{10}\text{Cu}_{31}\text{Sn}_4$ BMG exhibits a good combination of high mechanical properties, corrosion resistance (chemical biocompatibility) and is considered suitable for the production of alloys with high glass forming ability (GFA).

High strength Ti-based nanostructured/ultrafine eutectic composites present high fracture strength (~ 2000 - 2600 MPa) and larger plasticity ($>4\%$) compared with BMGs. One example is the Ti-Cu-Ni-Sn-Nb alloy composed of micrometric β -Ti dendrites in a nanostructure matrix, which exhibits a high strength of 2400 MPa and a plastic strain to fracture of $\sim 15\%$ [2]. Usually mechanical properties of alloys can be improved by microstructure refinement, as shown for hypoeutectic, eutectic or hypereutectic Ti-Fe-based alloys, consisting of primary phases and TiFe + β -Ti eutectic constituents exhibiting better mechanical properties (strength ~ 2200 MPa, plasticity $\sim 7\%$) and modified with elements such as Sn, Co and Nb [4-7].

The strength of conventional crystalline alloys follows the Hall-Petch relation, which predicts an increase in the strength when the grain sizes are decreased. Ti-based alloys with low density, high strength and ductility, as well as high chemical stability are of particular interest to energy efficient constructions. The ductility of nanostructured materials can be improved by embedding a submicron soft phase into a quasicrystal or nano-sized second phase [4–8]. Researchers have reported on the formation of complex phases and hardening mechanisms for supersaturated β -Ti solid solutions including phase separation [9-12] and

ultrafine structure composed by β -Ti/TiFe eutectic in Ti-based ultrafine composite alloys [11-15].

Metallic alloys used as biomaterials have much higher elastic modulus (E) than the one from human bone ($E = 10$ to 30 GPa): Stainless Steel (200 GPa), Co-Cr Alloys (220 GPa), Ti-6Al-4V (110 GPa) and the search for alloys with enhanced mechanical and chemical biocompatibility are required [16]. Some metallic Ti-based systems exhibited an unbalanced combination of elastic modulus and strength, for instance the Ti-Nb-Zr-Ta system, which shows rather low elastic modulus (i.e., good biomechanical compatibility with bone), but moderate hardness. On the contrary, the Ti-Fe-Sn system shows high yield strength, but also exceedingly high elastic modulus, which could eventually lead to stress shielding effects [17].

In the case of Ti-Fe-Sn, the deformation behavior of ultrafine composites is not fully understood due to the number of possibilities concerning the microstructure formation, which can be very complex. For instance, the alternation of microstructure features due to the variation in solute content may be very significant [17-19]. Moreover, Das and co-authors [6] affirm that Ti-Fe-Sn ultrafine eutectic composite is effective to change the growth of the eutectic phases and destabilize their morphology. Selecting the primary dendrite phase is a key factor to enhancing mechanical behavior. The effects of the cooling rate during rapid solidification on the obtained microstructure configuration of the Ti-Fe-Sn base alloys, however, remain undetermined.

Recently, Han et al. [20] investigated the ultrafine eutectic $(\text{Ti}_{65}\text{Fe}_{35})_{100-x}\text{Sn}_x$ alloys with $x=0, 1$ and 3 at%. The presence of Sn was reported as essential to control not only the dendritic array, but also to decrease the length-scale of the eutectic spacing. Nano-eutectic composites formed as part of the microstructure of Fe-Sn-Ti [21] were reported as having two distinct eutectic structures. The literature reveals a lack of understanding concerning fast cooling processes of Ti-Fe-Sn based alloys, including growth and competition between dendrites and eutectic microstructures. Research in this field would be very helpful to modulate the mechanical properties of these eutectic composites.

Up to now, research on the Sn and Nb combined modified microstructure and mechanical properties for eutectic Ti-Fe base alloys are still restricted. Therefore, the aim of this study is to investigate the microstructure features of the Ti-Fe-Nb-Sn alloys under different processing routes, i.e., *i.* fabrication of bulk plates by suction casting in copper mold and *ii.* laser melting of a pre-deposit powder alloy on a Ti substrate. Emphasis is given to studying the correlations between the microstructures and cooling rates, which are calculated for the different conditions adopted during both processing routes. The influences of microstructures and dilutions of elements (in the case of lasers) on hardness and on elastic modulus are also investigated.

2. Experimental procedure

Arc-melter equipment was used to prepare around 50g of the $\text{Ti}_{63}\text{Fe}_{23}\text{Nb}_8\text{Sn}_6$, $\text{Ti}_{60}\text{Fe}_{23}\text{Nb}_8\text{Sn}_9$ and $\text{Ti}_{66}\text{Fe}_{20}\text{Nb}_8\text{Sn}_6$ (at%) alloys by using high-purity constituent elements, i.e., Ti (99.9%), Nb (99.8%), electrolytic Fe (99.7%) and Sn (99.99%) in a Ti-gettered high-purity argon atmosphere. Samples of each alloy of 15g were cut from the ingots and further processed in a Discovery® suction casting system equipped with a copper mold. The copper mold designed in a plate shape, with varied thicknesses, had dimensions of 20×50 mm². Plates that are 0.5, 1.0, and 2.0mm thick were obtained. Details concerning the used casting assembly may be found in Fig. 1(a) by observing the so-called processing route (a).

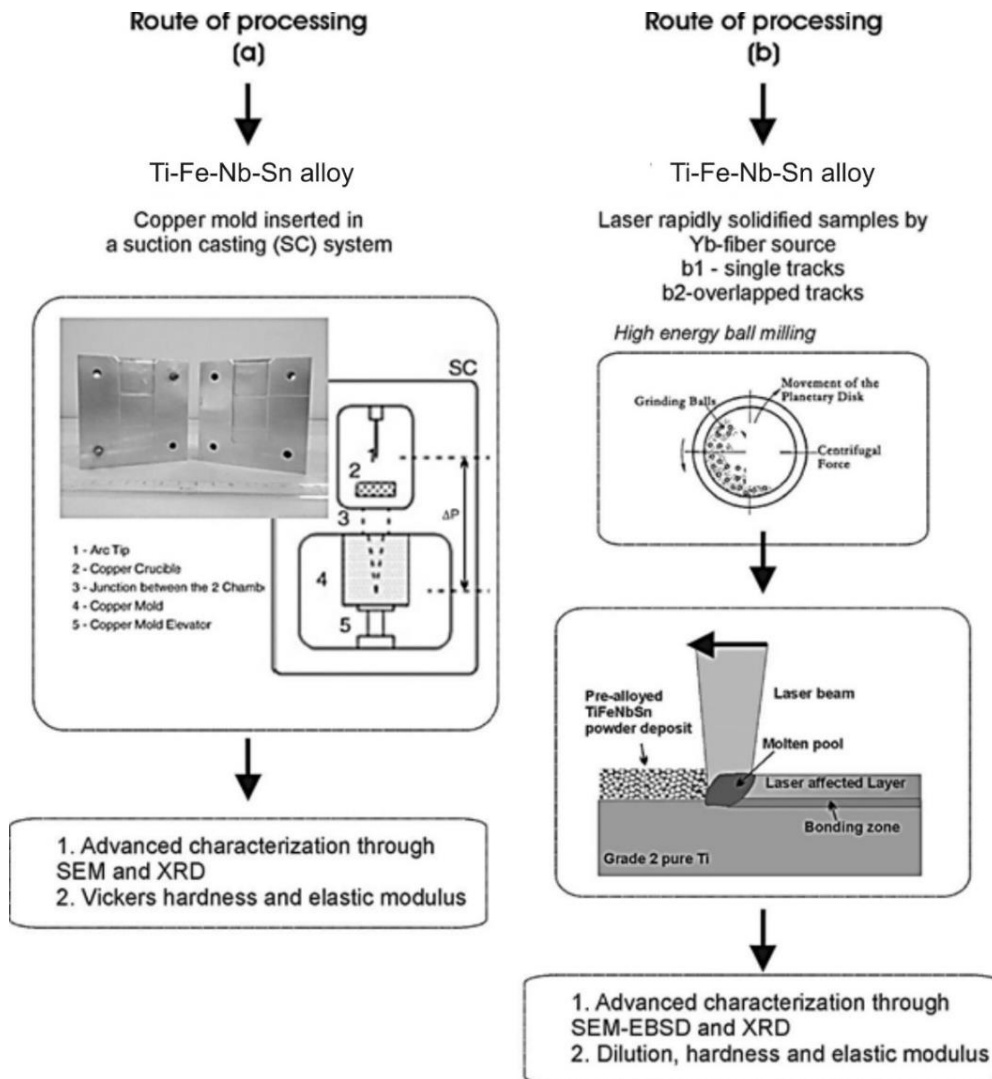


Fig. 1. Sequence of processing steps carried out in the Ti-Fe-Nb-Sn alloys: (a) rapid solidification by copper mold in suction casting apparatus followed by a comprehensive microstructural characterization; (b) powder preparation to permit laser melting to be performed following two conditions, which are: single tracks and overlapped tracks (resultant coatings).

The other processing route, as illustrated in Fig. 1(b) includes, firstly, an elemental mixture of the selected $Ti_{66}Fe_{20}Nb_8Sn_6$ alloy powders with a mass of around 100 g. These compositions were obtained by an elemental combination of pure Ti powder (99.5%/~100 μm in size), pure Nb powder (99.8%/~50 μm in size), gas atomized Fe-20Nb (wt.%) master alloy (<180 μm in size) and impulse atomized Sn-0.7Cu (wt.%) powder alloy (size range of 106-180 μm). Secondly, a high-energy ball milling (HEBM) processing step for the production of pre-alloyed and homogenized powders was performed by using a planetary mill for 2 h. Finally, a substrate of c.p. Ti of 2mm of thickness containing a pre-placed 500 μm thick layer

of the ball milled powder of the $Ti_{66}Fe_{20}Nb_8Sn_6$ alloy onto its surface was melted by laser cladding. For this purpose, a Yb- fiber laser (IPG, YLS2000) with an emitted radiation wavelength of $\lambda=1070nm$ and maximum power of 2000W was used. The laser beam was transmitted via an optical fiber of 100 μm of diameter to a 160 mm focal length lens. In this configuration, the laser beam diameter in the focus position was 100 μm . The samples were attached to a CNC XY table. In this study, the whole set of experiments was conducted with the sample surface positioned 8mm below the focus lens. The laser beam in this out-of-focus position presented a quasi-Gaussian profile with a diameter of 1 mm [22].

The laser melting experiments were carried out using single tracks and overlapped tracks (coatings) using different laser beam power, scanning speed and beam overlapping distance. A summary including the examined alloys, techniques and laser parameters adopted in the present investigation can be seen in Table 1.

Table 1. Studied alloys and main parameters used during laser cladding of the Ti-Fe-Nb-Sn alloys.

| Suction casting | Single track laser * | | | Overlapped tracks laser ** | | |
|--------------------------|--------------------------|--|-----------------------------|----------------------------|--------------|-----------------------|
| | Alloy | Scanning speed (mm/s) | Power (W) | Alloy | Power (W) | Scanning speed (mm/s) |
| $Ti_{66}Fe_{20}Nb_8Sn_6$ | $Ti_{66}Fe_{20}Nb_8Sn_6$ | 16.7, 33.3, 66.7, 100, 150 | 200, 400, 600, 800 | $Ti_{66}Fe_{20}Nb_8Sn_6$ | LC-1: 800 | 33.3 |
| | | | | | LC-2: 600 | 33.3 |
| | | | | | LC-3: 600 | 16.7 |
| $Ti_{60}Fe_{23}Nb_8Sn_9$ | | | | | LC-4: 400 | 16.7 |
| $Ti_{63}Fe_{23}Nb_8Sn_6$ | | | | | LC-5: 200 | 16.7 |

* Single tracks were performed for each combination of power, P (W) and scanning speed, Vb (mm/s).

** 50% (single track width) of superposition of tracks.

Bulk alloys, laser processed single tracks and coatings (overlapped tracks) specimens of the Ti-Fe-Nb-Sn alloys were submitted to microstructure characterization using X-ray diffraction (XRD), scanning electron microscopy (SEM) coupled to energy dispersive

spectroscopy (EDS), as well as EBSD analysis, which was used to characterize the laser processed coatings, their microstructures and formed crystalline phases. XRD measurements were performed on a Siemens diffractometer, model D5005 using Cu-K α radiation ($\lambda = 1.5418 \text{ \AA}$) and 1°/min scanning from 20 to 90° degrees (2 θ). A Field Emission Gun (FEG) - Scanning Electron Microscope (SEM) Philips (XL30 FEG) coupled to an Energy Dispersive Spectroscopy - EDS (Oxford Link ISIS 300) was used. Furthermore, a SEM-EDS FEI (Inspect S50L) was required to complete the analyses. Vickers microhardness tests were performed by using test loads of 50g, 300 g and 1000g and a dwell time of 10s using a Stiefelmayer KL2 model hardness test device.

Nanoindentation tests were conducted after a previous study of the tracks and coatings, so that those with better characteristics (low dilution, homogenization, and an acute angle between track and substrate) were selected for this assay. The nanohardness (GPa) and elastic modulus (GPa) of the laser processed samples were measured introducing the samples in the machine Nano Indenter G200 the night before the tests in order to establish an adequate thermal equilibrium between the sample and machine. The elastic modulus of the selected bulk alloy was obtained from mechanical spectroscopy tests described in detail previously [23], using free decay elastometer equipment (Vibran Technologies AE-102) from the logarithmic decay of free oscillations of the first tone in flexural vibration mode.

3. Results and discussion

3.1. Rapid solidification of bulk Ti-Fe-Nb-Sn alloys through copper mold casting

Fig. 2 depicts the XRD patterns of the Ti₆₃Fe₂₃Nb₈Sn₆ and Ti₆₆Fe₂₀Nb₈Sn₆ alloys composed mainly of β -Ti matrix and TiFe intermetallic phases (for the further alloy) and, additionally the Ti₃Sn phase that appears for the further alloy. The ultrafine eutectics Ti₆₃Fe₂₃Nb₈Sn₆ and Ti₆₆Fe₂₀Nb₈Sn₆ (at%) alloys showed very sharp and high intensity peaks, typical of eutectic ultrafine composites or even nanocrystalline metallic structures.

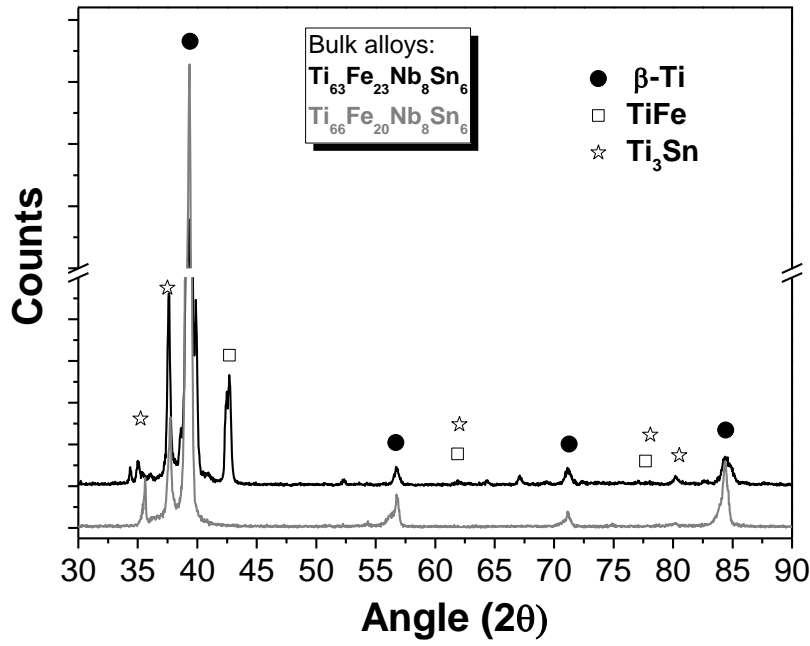


Fig. 2. XRD patterns of $Ti_{63}Fe_{23}Nb_8Sn_6$ and $Ti_{66}Fe_{20}Nb_8Sn_6$ (at%) alloys composed mainly of the β -Ti matrix and TiFe intermetallic phase ($Ti_{63}Fe_{23}Nb_8Sn_6$ alloy) and, additionally the Ti_3Sn phase that appears for the $Ti_{63}Fe_{23}Nb_8Sn_6$ (at%) alloy.

Fig. 3 shows SEM microstructures (BSE) of $Ti_{66}Fe_{20}Nb_8Sn_6$ alloy for plates with thicknesses of 0.5mm and 1.0mm. In both cases, the β -Ti phase (BCC) in the form of dendrites can be observed, which probably contains Nb and Fe in the solid solution and intermetallic particles precipitated within the interdendritic regions. The results from XRD in Fig. 2 reveal that there is a predominance of Ti_3Sn intermetallic developed in such regions due to much higher peak intensities corresponding to this phase. Finer dendrites can be observed for the finer plate of $t=0.5$ mm. This microstructure development is due to the higher cooling rates during solidification in smaller plate thicknesses, which happens basically due to the thicker copper-mold wall, followed by a reduction in the cooling rate as a function of increasing the plate thickness. According to the equation proposed by Lin and Johnson [24], the cooling rate in multicomponent Ti alloy thin plates can be calculated as follows:

$$\dot{T} = \frac{k(T_m - T_0)}{C R^2}, \quad (1)$$

where k is the thermal conductivity, T_m and T_0 are the melting and room temperatures, respectively, C is the thermal capacity and R is the thickness of the plate.

Considering plates with 0.5mm, 1.0mm and 2.0 mm in thickness, cooling rate values of 3.9×10^4 , 9.7×10^3 and 2.4×10^3 K/s have been determined based on equation (1), respectively.

Vickers hardness (HV) and elastic modulus were determined for the $Ti_{66}Fe_{20}Nb_8Sn_6$ alloy plate with 1mm in thickness. An average indentation value of 417HV was determined (see Table 2), which can be considered low due to the presence of relatively coarse Ti-rich dendrites. However, this kind of microstructure configuration (dendrites of β -Ti enveloped by Ti_3Sn intermetallics) may lead to a suitable elastic modulus of 72GPa measured by mechanical spectroscopy. Chaves and co-authors [23] have recently determined an elastic modulus of 65GPa for a rapidly quenched β -type Ti-25Nb-3Fe (wt.%) alloy. In this case, a strong addition of β stabilizers is pointed out as being mainly responsible for reducing the elastic modulus. Indeed, the Nb content is considerably high, which could increase costs associated to adopting such an alloy for implants. The combination of low Nb-content and suitable elastic modulus found in the $Ti_{66}Fe_{20}Nb_8Sn_6$ alloy seems to be an attractive characteristic to use this alloy for biomedical purposes.

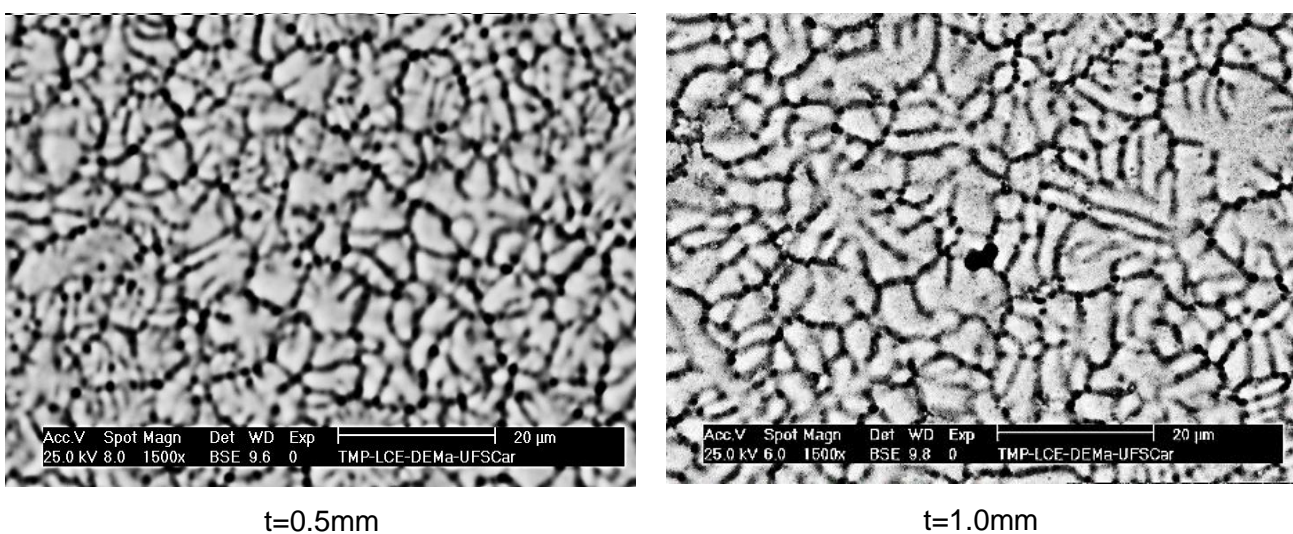


Fig. 3. Typical SEM images obtained for plates with different thicknesses (t) along the $Ti_{66}Fe_{20}Nb_8Sn_6$ (at%) alloy casting by suction casting facility.

Table 2. Vickers microhardness ($HV_{0.2}$) measurements for the ultrafine eutectics of $Ti_{63}Fe_{23}Nb_8Sn_6$, $Ti_{60}Fe_{23}Nb_8Sn_9$ and $Ti_{66}Fe_{20}Nb_8Sn_6$ (at%) alloys.

| Alloy (at.%) | ($HV_{1.0}$) |
|--------------------------|----------------|
| $Ti_{63}Fe_{23}Nb_8Sn_6$ | 488 ± 18 |
| $Ti_{60}Fe_{23}Nb_8Sn_9$ | 608 ± 3.0 |
| $Ti_{66}Fe_{20}Nb_8Sn_6$ | 417 ± 15 |

3.2. Features of the $Ti_{66}Fe_{20}Nb_8Sn_6$ powder alloy prepared by mechanical milling

Fig. 4 shows the curve representing the particle size distribution of the $Ti_{66}Fe_{20}Nb_8Sn_6$ powder used to process the single tracks and coatings. It can be considered a coarse powder with a high heterogeneity of particle sizes, which means that a mixture of particles with prevalence from sizes ranging from $33\mu m$ to $230\mu m$ was found. On average, the mean particle size was $d_{50} = 113.4\mu m$.

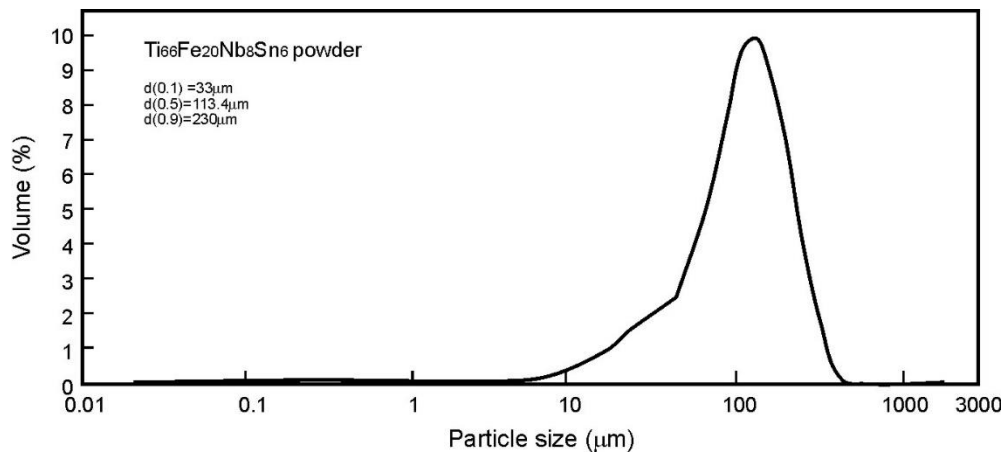


Fig. 4. Granulometric distribution of the $Ti_{66}Fe_{20}Nb_8Sn_6$ powder, processed by mechanical milling of elemental powders to be used as pre-placed material for Laser Cladding.

The resulting powder mixed through mechanical milling can be seen in Fig. 5. The large heterogeneity in particle sizes shown in the granulometric profile (Fig. 4) is confirmed by the SEM general view on the left side of Fig. 5.a. In addition, Fig. 5b depicts the presence

of very fine fragments of Nb and Sn-based powders which may be incorporated into larger particles due to the impacts and attritions involved during the mechanical milling process.

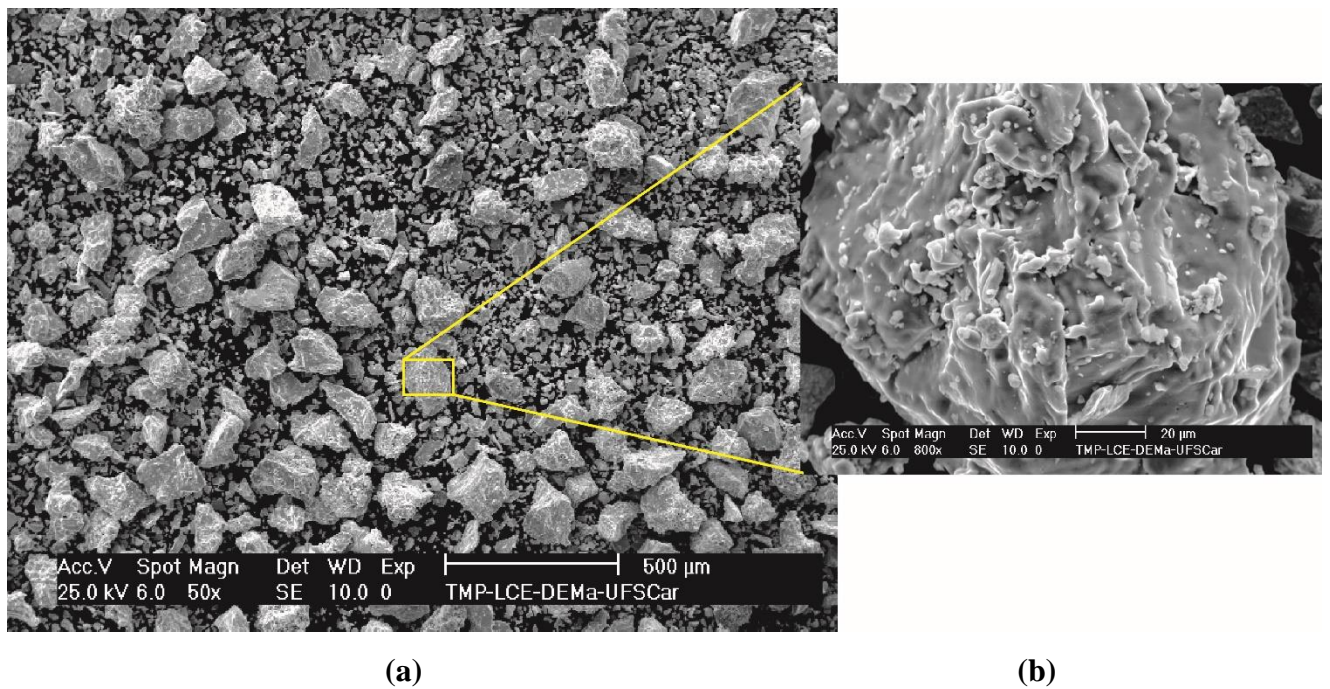


Fig. 5. (a) General and (b) detailed SEM microstructures of the pre-alloyed $Ti_{66}Fe_{20}Nb_8Sn_6$ powder used in laser process.

3.3. Evaluation of Laser Cladding single tracks of the $Ti_{66}Fe_{20}Nb_8Sn_6$ alloy

SEM images of selected samples in conditions tested by laser cladding were chosen to be depicted in Fig. 6 with general views of the formed molten pools in the left images (Figs. 6.a, 6.c, 6.e and 6.g) and detailed interfaces between molten and heat affected zones (HAZ) of $Ti_{66}Fe_{20}Nb_8Sn_6$ (at%) alloy on the right side (see Figs. 6.b and 6.d). Figs. 6.b and 6.d show the presence of epitaxial growth at the interface between melted and HAZ regions with aligned dendrites growing from the substrate, according to the heat extraction direction. The microstructures that solidified right next to the bottom of the treated pool experienced an epitaxial growth and certain alignment with the growth direction, while tens of microns ahead a non-aligned growth prevailed. On the other hand, for regions farther from the interface (e.g. $P=400W$ and $V_b=66.7mm/s$) in Fig. 6.h, a cell-to-dendritic transition can be observed.

During the laser cladding process, after the interruption of energy input in a specific section, melting continued, however briefly, before the onset of solidification. Thus, the cooling rates imposed and the solidification velocity at the bottom of the pool were both initially close to zero. The cooling rate started at zero and tended to be a constant value as solidification proceeded to the pool surface. The evolution of the microstructure depends on this variation of cooling rate. The presence of cells may be attributed to an increase in both the cooling rate and growth rate towards the surface of the pool. These cells are the so-called high-cooling rate cells [25-26].

Another feature to be considered is the presence of α' martensite in the unmelted zone, which can be considered as a heat affected zone (HAZ). The general views of the laser tracks on the left side of Fig. 6 suggest an inhomogeneous distribution of alloying elements due to the typical short interaction times. It is often considered that at high cooling rates, due to kinetic restrictions, there is not enough time for the atoms to arrange themselves in a stable structure [27]. The equation proposed by Ashby and Easterling [28] allowed for the cooling rate in laser melting traces to be estimated, based on the following expression:

$$\dot{T} = - \frac{2\pi k(T_m - T_0)^2}{A \left(\frac{q'}{v}\right)}, \quad (2)$$

where A is the absorptivity for the laser beam, v is the laser scanning speed, and q' is the corrected power considering losses generated by energy absorption as latent heat when the liquid forms. q' also depends on the laser beam radius and thickness of the melted layer. In the present research, q' was considered as being the average power of each tested condition. Based on the aforementioned equation, the cooling rate values inserted in Fig. 6 could be estimated. The cooling rates related to laser processing are at least one order of magnitude higher than those calculated for the thin $\text{Ti}_{66}\text{Fe}_{20}\text{Nb}_8\text{Sn}_6$ alloy copper mold cast plates.

In SEM (BSE) analyses, heavier phases in terms of the atomic number (Z) are able to backscatter electrons more strongly than light ones, and thus appear brighter in the microstructure (chemical contrast). Nb particles and Sn-rich layers can be seen in Figs. 6.a,

6.c, 6.e and 6.g appearing indicated by arrows as Nb and Sn are heavier elements if compared to Ti and Fe. As a pure Ti substrate is used, as soon as the energy input is started in a certain region of the pre-deposited powders, a dilution process may occur. A decrease in the concentration of niobium, iron and tin must prevail in regions near the interface with higher concentration of titanium at the interface. As well as the contribution of the formed compositional gradients within the molten pool, another particular fluid flow pattern may be induced during laser treatment. This flow seems to be able to fetch Sn and Nb upwards to the regions where higher solidification velocities must predominate. This is mainly for Sn, which shows a much lower melting temperature $T_m = 232 \text{ }^\circ\text{C}$ when compared to the Nb one ($T_m = 2469 \text{ }^\circ\text{C}$). This phenomenon of transport is induced by the Marangoni convection, also called surface-tension-driven convection, consisting of the development of eddies that produce high velocities (of the order of 1 m/s) compared to the natural convection (of the order of 1 mm/s) [29].

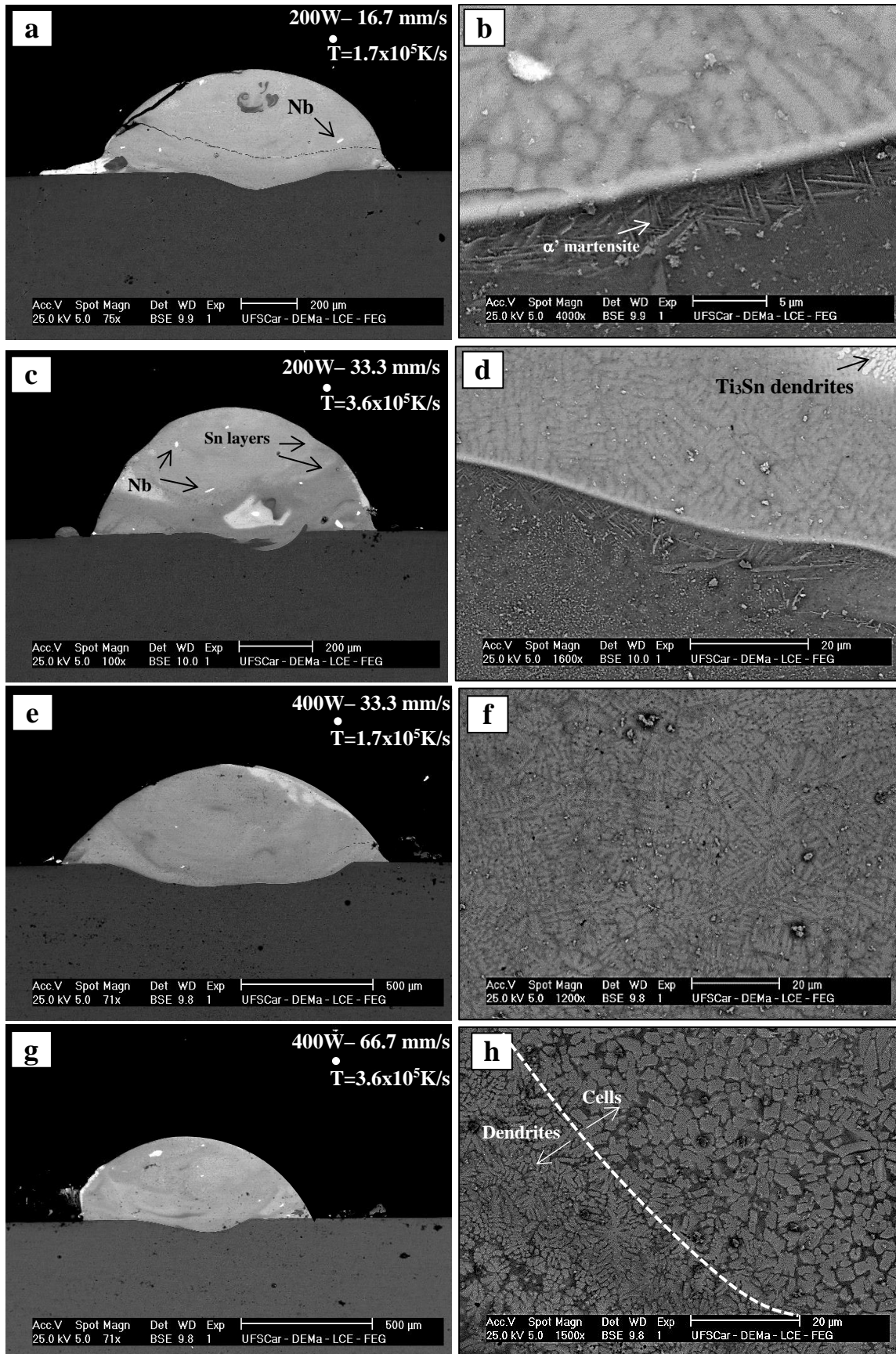


Fig. 6. Representative SEM micrographs showing: (a,c,e,g) general shape of the molten pool; (b,d) interface between single Laser affected traces of $\text{Ti}_{66}\text{Fe}_{20}\text{Nb}_8\text{Sn}_6$ (at%) alloy and the surface of the Ti substrate; and (f,h) the growth of dendrites and cells along the laser melted region. $P=200/400\text{W}$; $V_b=16.7/33.3/66.7\text{mm/s}$. \dot{T} is the cooling rate.

X-ray elemental mapping obtained by energy-dispersive spectroscopy (EDS) can reveal the compositional variations from the free surface of the pool to the substrate as can be seen in Fig. 7.

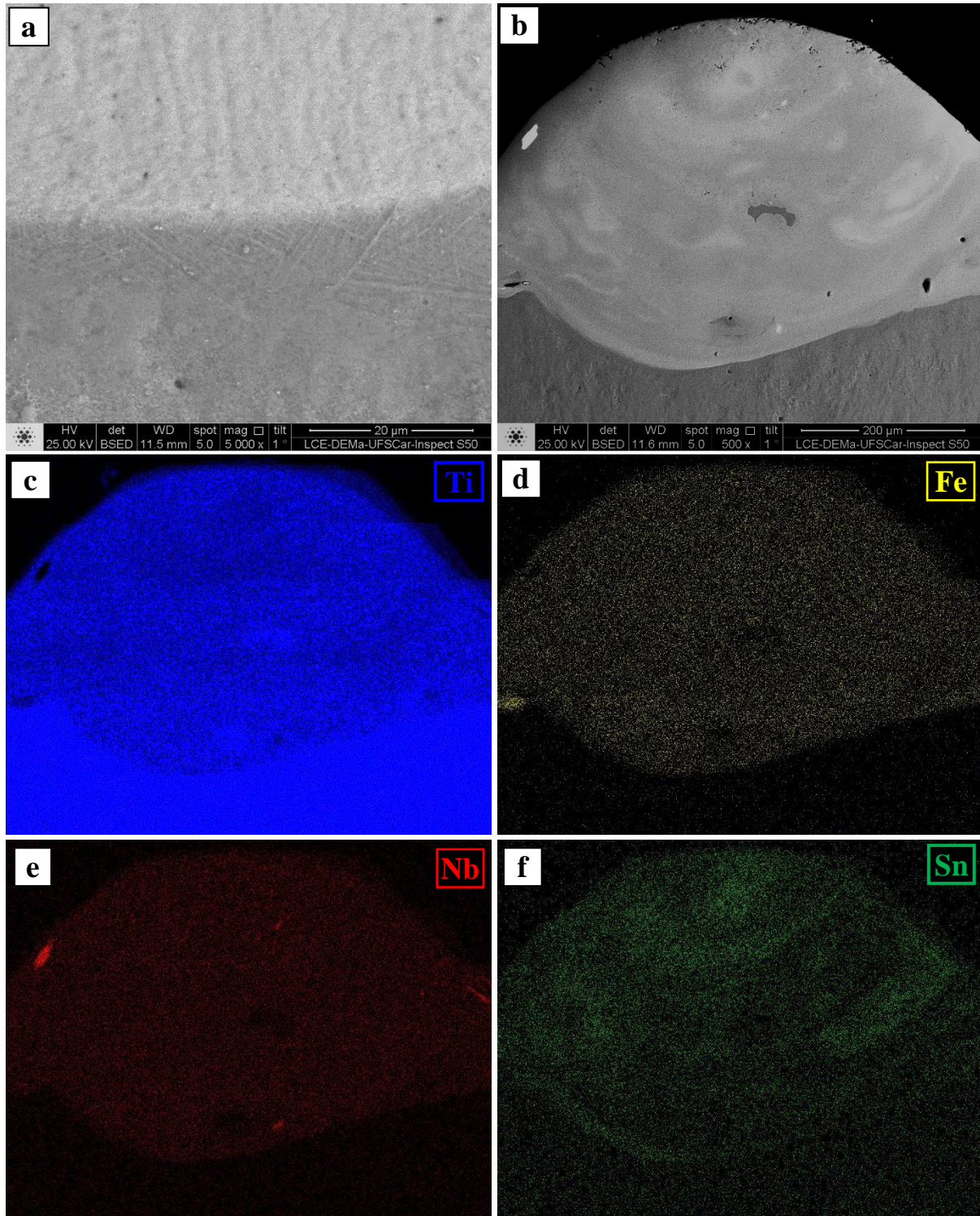


Fig. 7. (a), (b) SEM micrographs with features typically found in the interface between laser melted and heat affected zones (HAZ) of the $Ti_{66}Fe_{20}Nb_8Sn_6$ alloy, and respective X-ray elemental mapping obtained by EDS of (c) Ti-K, (d) Fe-K, (e) Nb-L and (f) Sn-L.

The X-ray mapping by SEM-EDS shown in Fig. 7 confirms the non-uniformity of the material, depending on the laser cladding parameters adopted. Lighter areas are Sn-enriched in Fig. 7.b and correspond to green regions in Fig. 7.f. Very high cooling rates imposed during laser cladding do not provide enough time for complete melting and homogenization of the molten pool. Sn-rich regions favor the formation of Ti_3Sn primary dendrites, as can be seen in Fig. 6b, shown by the black arrow. A high fraction of the Ti_3Sn phase can be seen in Fig. 8, with dendritic growth near the surface of the pool and the growth of such dendrites concurs with the Sn-rich layers observed in Fig. 6 and Fig. 7.

Lee and co-authors [18] investigated ultrafine Ti-Fe-Sn eutectic by increasing the concentration of Sn and examining microstructure changes. The growth of micro-scale Ti_3Sn dendrites uniformly embedded in the TiFe and β -Ti eutectic structure for the $Ti_{68}Fe_{23}Sn_9$ alloy is stressed, whereas β -Ti primary dendrite in eutectic matrix was found for the $Ti_{72}Fe_{22}Sn_6$ alloy. According to this research, the Ti_3Sn dendrites may lead to slip bands that induce work hardening playing a fundamental role in plasticity during deformation. Zhang and collaborators [19] stated that the structural incompatibility between Ti_3Sn and bcc FeTi and β -Ti blocks the dislocation transfer across their interfaces, which accelerates the failure around the Ti_3Sn phase.

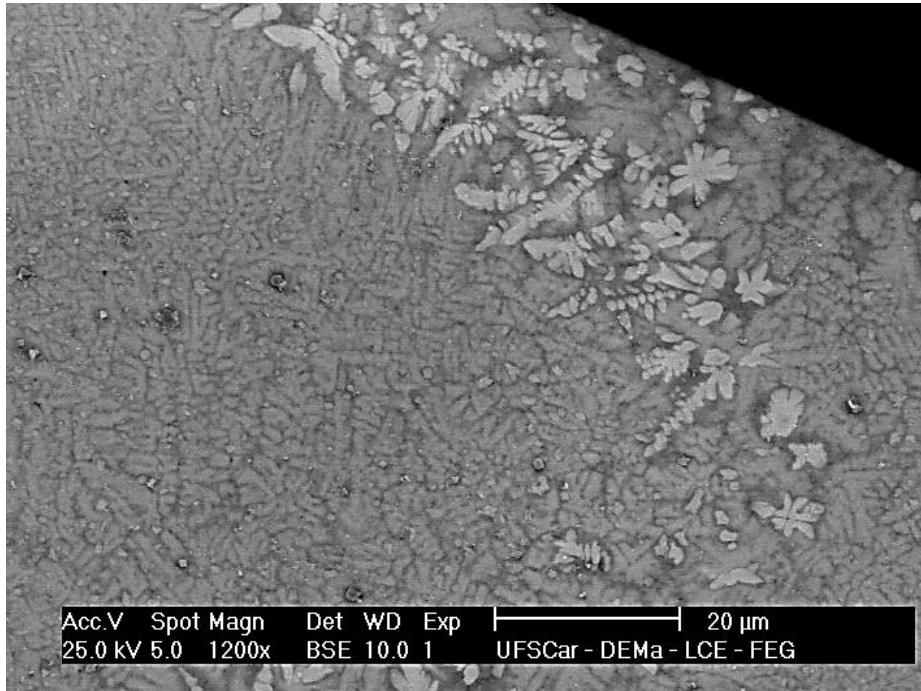


Fig. 8. SEM microstructure of the $Ti_{66}Fe_{20}Nb_8Sn_6$ alloy emphasizing the presence of fine primary Ti_3Sn dendrites (brighter phases) in the molten pool obtained using the laser process with $P=200W$ and $V_b=16.7mm/s$.

If a single laser power is considered, two different experimental trends for hardness vs power density can be seen in Fig. 9. For low power densities, hardness increases with increasing laser power density (PD). As a certain PD value is achieved, a reverse behaviour starts to happen with decreasing hardness values. If lower laser powers of 200W and 400W are considered, it seems that for low PD values, dilution involved in the process is inhibited and, as a consequence, depletion of the elements such as Nb, Fe and Sn at the unmelted/melted interface is partially avoided. As PD is increased for the processing condition associated with 400W, dilution takes place and, as a consequence, hardness diminishes. In the case of $P=800W$ and $P=1000W$, a slight reverse is noted in the hardness evolution, decreasing with increasing PD values. For power densities higher than $10 J/mm^2$, higher laser power leads to lower hardness values. According to the cooling rate equation proposed by Ashby and Easterling (Equation (2)), an increase in laser power results in a decreasing cooling rate. Thus, lower hardness values may be explained due to the more

diluted compositions of track and coarser microstructures formed as a consequence of relatively slower cooling conditions during laser cladding.

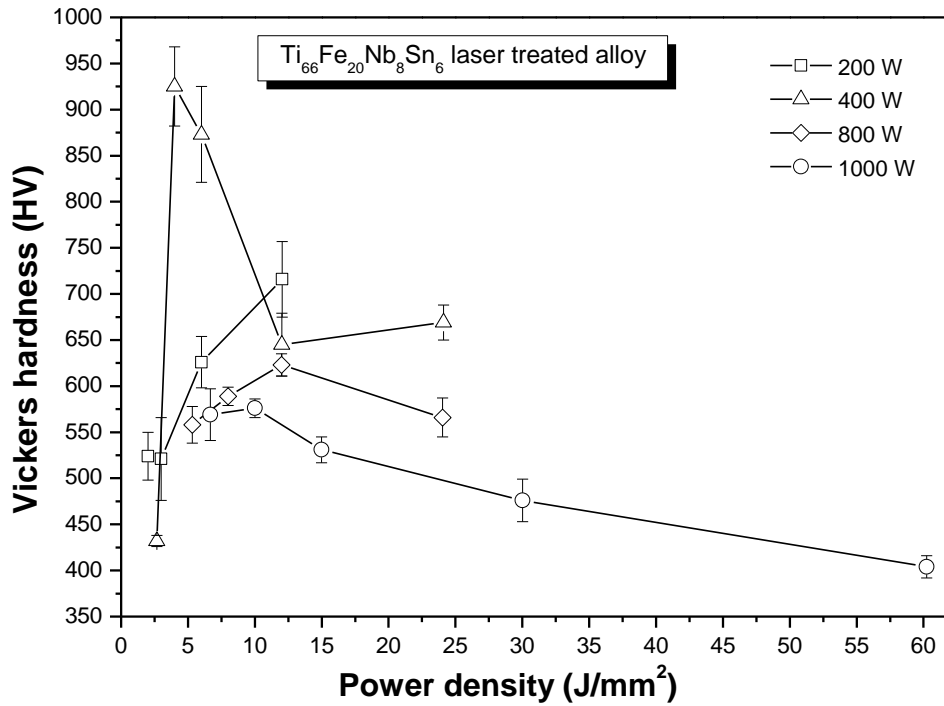


Fig. 9. Evolution of Vickers microhardness measured at the cross section of the Laser tracks as a function of power density (PD) for the $Ti_{66}Fe_{20}Nb_8Sn_6$ alloy.

High elastic modulus values were determined for the $Ti_{66}Fe_{20}Nb_8Sn_6$ alloy single tracks corresponding to 400W/33.3mm/s and 200W/16.7mm/s. Both process conditions resulted in a modulus around 145GPa, which is 2 times higher than that obtained for the bulk alloy. Greater values of Vickers microhardness (HV) appeared for lower laser power values and higher scanning speeds (lower PDs), such as the combination of 925 ± 44 HV for 400 W, 100 mm/s (4 J/mm^2 in graph of Fig. 9 – triangles symbols), respectively. On the other hand, this combination of parameters might result in intense residual stress and lead to cracks across the laser track transversal section. Lower scanning speeds and higher laser power values (higher PDs) lead to greater dilutions of pre-alloyed powders (coatings with more homogenous composition), but lower contents of alloying elements, and consequently, a lower fraction of hard intermetallic phases ($TiFe$ and Ti_3Sn), resulting in lower values of microhardness measured.

3.4. Coatings generated by Laser Cladding of the $Ti_{66}Fe_{20}Nb_8Sn_6$ alloy

After analysing the laser cladding tracks, the best combination of laser parameters for the production of coatings was selected based on power, P (W), laser beam scanning speed V_b (mm/s), and results obtained in terms of: microhardness (HV), better composition homogeneity of clad track (better laser alloying conditions avoiding particles, or regions, enriched in one specific element: Nb, Fe and Sn) and lower dilution maintaining composition of coating similar to that of the nominal original powder composition $Ti_{66}Fe_{20}Nb_8Sn_6$.

A selected combination of laser cladding parameters was used to produce overlapped tracks. Fig. 10 shows XRD patterns of laser cladding coatings of pre-alloyed powders of $Ti_{66}Fe_{20}Nb_8Sn_6$ alloy for different combinations of laser cladding parameters: power (W) and V_b (mm/s), following the nomenclature given in Table 1.

It can be observed from the XRD patterns that the phases formed in the coating strongly depend on the combination of laser cladding parameters. The intermetallic TiFe phase (combined with β -Ti matrix and Ti_3Sn phase) was clearly formed only for lower laser power (200 W) and lower scanning speed (16.7 mm/s) for the coating LC-5 (green line). In general, all the other conditions using higher laser power (400, 600 and 800 W) lead to the formation and identification of only Ti_3Sn intermetallic and β -Ti matrix. It is likely that the laser parameters will lead to dilution conditions away from the eutectic β -Ti + TiFe composition, avoiding or minimizing the formation of the intermetallic TiFe phase, in which precipitation was preferred over the copper mold cast $Ti_{63}Fe_{23}Nb_8Sn_6$ and $Ti_{60}Fe_{23}Nb_8Sn_9$ (at%) alloys in XRD patterns in Fig. 2 and Table 2 with higher Fe additions.

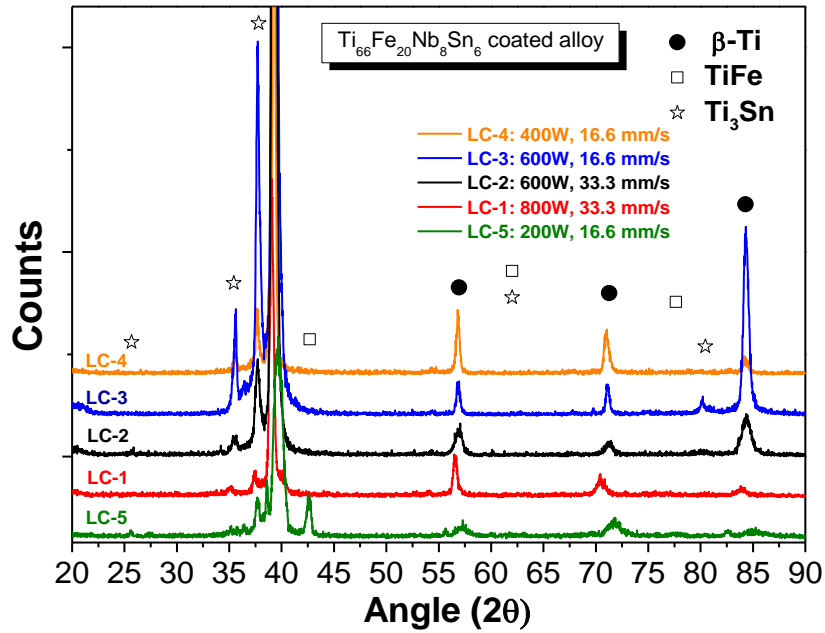


Fig. 10. XRD patterns of coatings generated from laser cladding of pre-alloyed powders of $Ti_{66}Fe_{20}Nb_8Sn_6$ alloy for different combinations of laser cladding parameters.

Fig. 11 shows SEM micrographs of typical coatings obtained by laser cladding of pre-alloyed powders of $Ti_{66}Fe_{20}Nb_8Sn_6$ alloy for selected combinations of laser parameters: $P = 800W$, $V_b = 33.3$ mm/s (Fig. 11.a); $P = 600W$, $V_b = 16.7$ mm/s (Fig. 11.b); $P = 400W$, $V_b = 16.7$ mm/s (Fig. 11.c); $P = 200W$, $V_b = 16.7$ mm/s (Fig. 11.d). Although the higher laser power used in Fig. 11.a ($P = 800W$) may lead to a deeper penetration of laser beam and, consequently, higher dilution, composition homogeneity of the coating resulted poor, showing flux lines with compositional variations due to chemical contrast (Z). As the laser power decreases in Figs. 11.b and 11.c ($P = 600$ and 400 W, respectively), the coating dilution diminishes leading to better composition homogeneity, and the precipitation of Ti_3Sn intermetallic becomes more significant, in agreement with the XRD patterns (Fig. 10). It can be confirmed in the SEM images in BSE mode (Fig. 11.d) that the coexistence of TiFe and Ti_3Sn intermetallic phases combined with β -Ti matrix only appeared for the coating LC-5 (green line in Fig. 10) with lower laser power (200 W) and a scanning speed (16.7 mm/s).

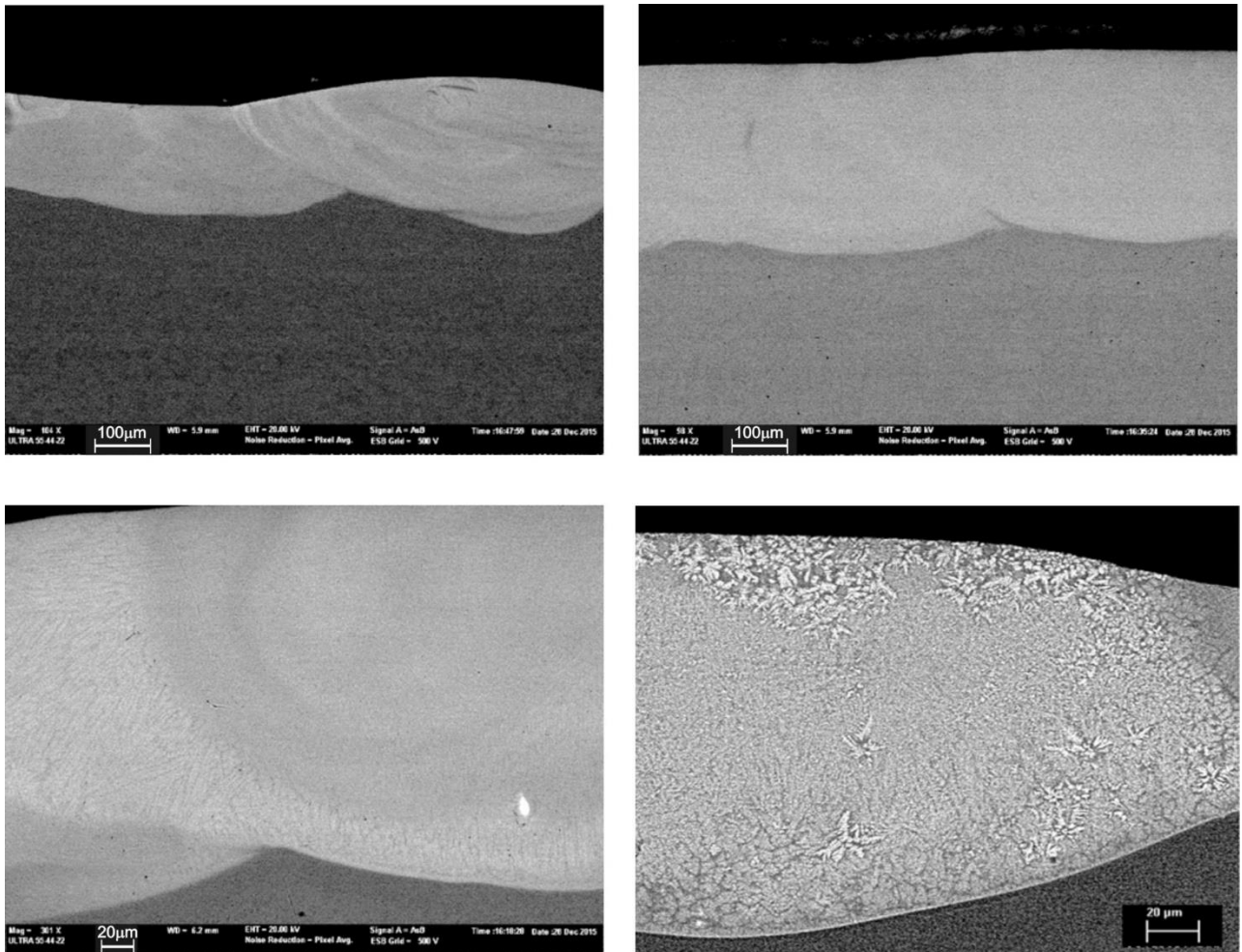


Fig. 11. SEM micrographs of typical coatings profiles obtained by laser cladding of pre-alloyed powders of $\text{Ti}_{66}\text{Fe}_{20}\text{Nb}_8\text{Sn}_6$ alloy for selected combinations of laser parameters: (a) 800W (33.3 mm/s) – LC-1; (b) 600W (16.7 mm/s) – LC-3; (c) 400W (16.7 mm/s) – LC-4; (d) 200W (16.7 mm/s) – LC-5.

Fig. 12 shows EBSD patterns obtained in SEM for the laser clad coatings of $\text{Ti}_{66}\text{Fe}_{20}\text{Nb}_8\text{Sn}_6$ pre-alloyed powders using lower scanning speed (16.7 mm/s) in the LC-5 sample with laser power of 200 W showing inverse pole figure (IPF-colouring) with different orientations (Fig. 12.a) and an EBSD phase map (Fig. 12.b) showing dendritic Ti_3Sn (red) and a TiFe intermetallic phase (yellow) dispersed in the β -Ti matrix (blue). Combined SEM-EDS X-ray maps show the distribution of elements Fe (Fig. 12.c) and Sn (Fig. 12.d) through the coating's microstructure processed at 200 W and 16.7 mm/s (1 m/min).

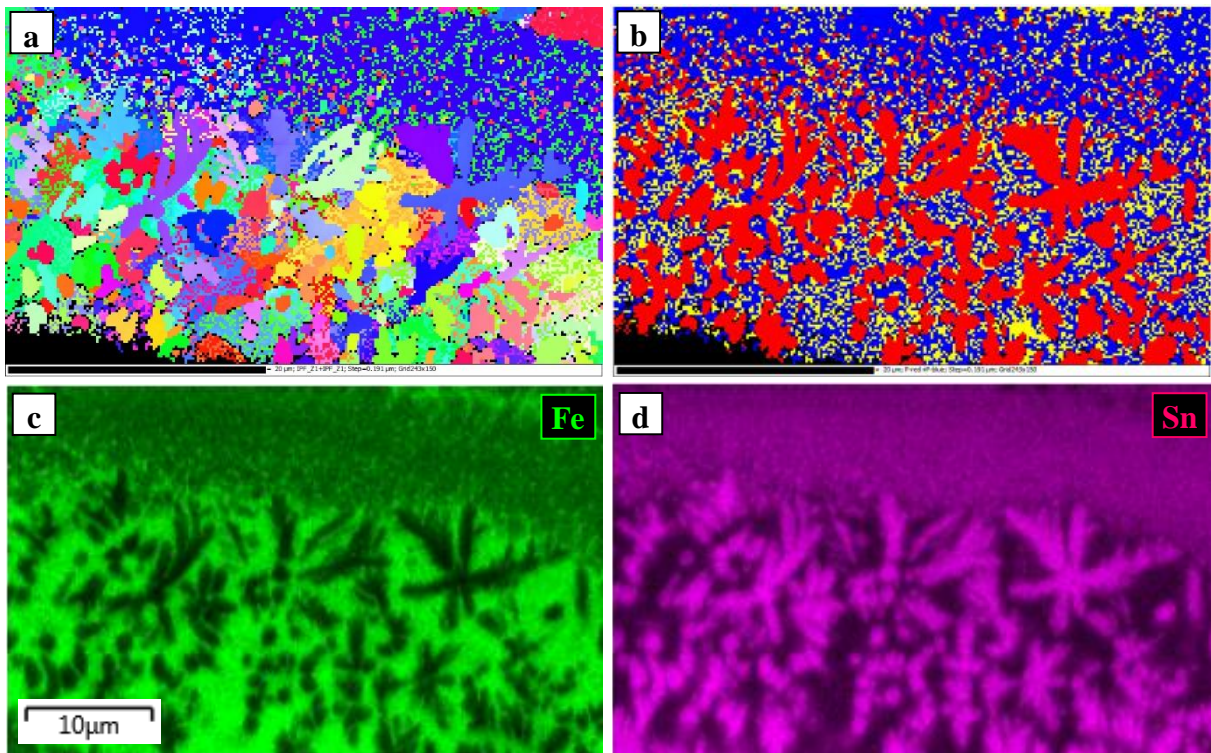


Fig. 12. SEM-EBSD results for laser clad coatings of $\text{Ti}_{66}\text{Fe}_{20}\text{Nb}_8\text{Sn}_6$ alloy (condition LC-5) based on (a) IPF-colouring with different orientations and (b) EBSD phases maps. Elemental distributions of (c) iron (Fe) and (d) tin (Sn) along the microstructure regarding the coated zones.

Fig. 13 shows a graph with SEM-EDS linescan semi-quantitative composition along the interface coating/ Ti substrate processed with power of 600 W and speed of 33.3 mm/s. It is a representative case showing that the application of high laser power to generate the T-Fe-Nb-Sn/Ti coating may lead to higher dilution and composition inhomogeneity in relatively large distances from the substrate/deposit interface. The more uneven case refers to the Sn distribution profile in Fig. 13.

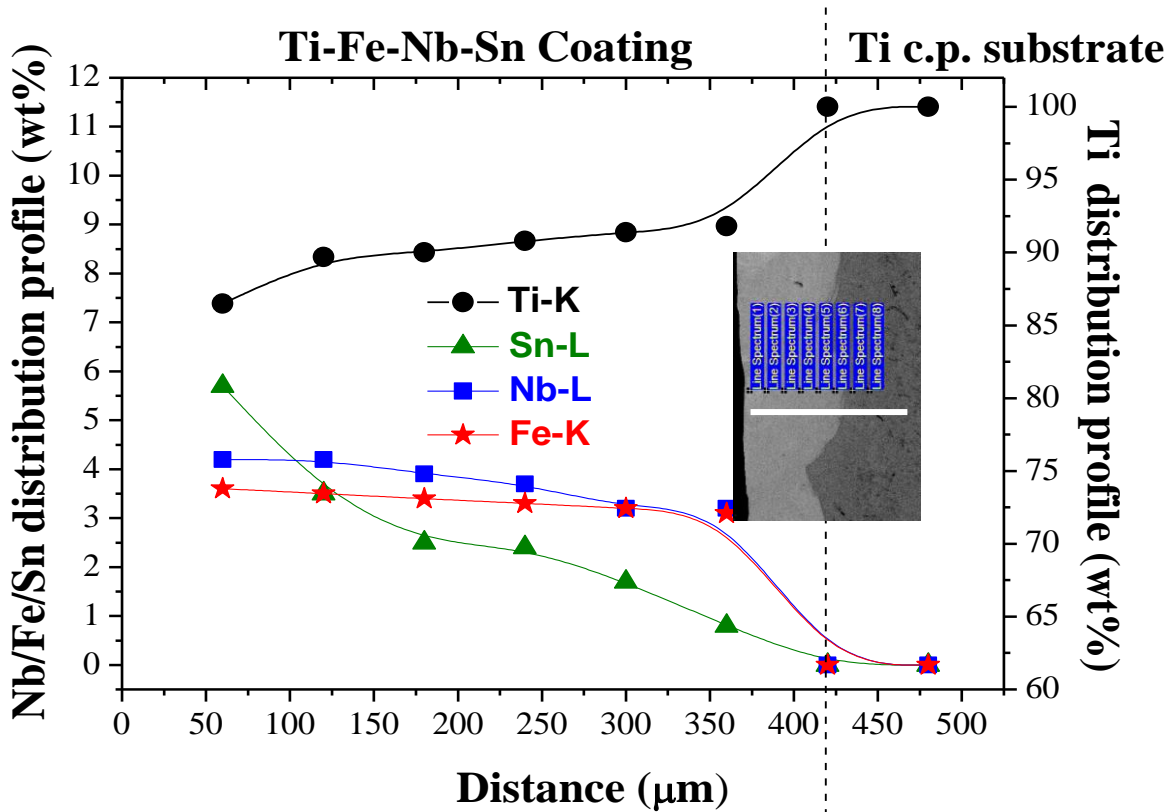


Fig. 13. Graphs showing semi-quantitative compositions through SEM-EDS linescan along the interface between the Ti-Fe-Nb-Sn coating and the Ti substrate processed with power of 600 W and scanning speed of 33.3 mm/s (condition LC-2).

Table 3 shows the Vickers microhardness values for laser clad tracks and nanohardness values (GPa) and elastic modulus (GPa) for the respective coatings with the same combination of laser parameters, power (W) and scanning speed (mm/s) for $Ti_{66}Fe_{20}Nb_8Sn_6$ (at%) produced by Laser Cladding onto Ti substrate. As a reference, values of the same properties are shown for the c.p. Ti and Ti-6Al-4V alloy to compare the values obtained in this work.

According to the microhardness (HV) values obtained for laser clad tracks (589 – 716 $HV_{0.3}$) depending on the laser parameters (laser power and scanning speed) imposed, it can be concluded that the hardness was very high when compared to the commercial c.p. Ti with 160 – 200 HV and Ti-6Al-4V with 220 HV [17]. Usually, β -Ti alloys present microhardness values between 200 and 300 HV near the stabilization of β phase (bcc), other Ti-based systems such as Ti-Cu alloys show microhardness values in the range of 220 to 380 HV [13]

and eutectic Ti-Fe presented high values of 480 to 630 HV [14]. Even for the very hard Ti-based metallic glasses (BMG), the values reached up to 710 HV for $(\text{Ti}_{40}\text{Zr}_{10}\text{Cu}_{36}\text{Pd}_{14})_{100-2x}\text{Si}_x$ alloys [30], comparable with the values obtained in this work of 716 HV.

Table 3. Vickers microhardness values for laser clad tracks and respective coatings with the same combination of laser parameters, power (W) and scanning speed (mm/s) for $\text{Ti}_{66}\text{Fe}_{20}\text{Nb}_8\text{Sn}_6$ (at%) and resulting values of nanohardness and elastic Modulus (GPa).

| Power [W] | Scanning Speed [mm/s] | Vickers Microhardness ($\text{HV}_{0.3}$) | Nanohardness (GPa) | Elastic Modulus (GPa) | Ref. |
|-----------|-----------------------|---|--------------------|-----------------------|------------------|
| 200 | 16.7 | 716 ± 41 | 6.5 ± 0.4 | 130 ± 41 | <i>This work</i> |
| 400 | 33.3 | 669 ± 19 | 8.0 ± 0.2 | 148 ± 19 | <i>This work</i> |
| 600 | 16.7 | 623 ± 12 | 4.8 ± 0.2 | 98 ± 12 | <i>This work</i> |
| 800 | 33.3 | 645 ± 34 | 6.4 ± 0.3 | 133 ± 34 | <i>This work</i> |
| 800 | 150 | 589 ± 10 | 7.0 ± 0.1 | 130 ± 10 | <i>This work</i> |
| c.p. Ti | — | 160 – 200 | 2.3 ± 0.2 | 126 ± 28 | <i>This work</i> |
| Ti-6Al-4V | — | 220 | 5.0 ± 0.1 | 121 ± 3 | [17] |

Comparing the microhardness of clad tracks processed by laser cladding with the value obtained in a 1mm thick plate of $\text{Ti}_{66}\text{Fe}_{20}\text{Nb}_8\text{Sn}_6$ alloy (417 HV) processed by copper mold casting, there was a significant hardness increase up to 72%. Such an increase may be devoted to the much higher cooling rates obtained via laser cladding such as that microstructure resulted very refined with nanoscale intermetallic precipitates combined with hard Ti_3Sn dendrites embedded in a β -Ti matrix. Fig. 14 shows variations of Nanohardness (GPa) and Elastic Modulus (GPa) values for coatings produced by laser cladding of $\text{Ti}_{66}\text{Fe}_{20}\text{Nb}_8\text{Sn}_6$ (at%) pre-alloyed powder for different combinations of laser parameters, power, P (W) and scanning speed, V_b (mm/s).

The coatings produced by laser alloying of pre-placed $\text{Ti}_{66}\text{Fe}_{20}\text{Nb}_8\text{Sn}_6$ (at%) elemental powders lead to varied values of nanohardness (4.8 – 8.0 GPa) and elastic modulus (98 – 150 GPa) depending on the laser parameters (power and scanning speed) imposed. In comparison

to such ranges of values, the elastic modulus of the eutectic binary Ti-Fe determined from nanohardness measurements was 137 GPa [9,10,13,14], while modulus of β -Ti alloys usually rely on the range of 55 to 80 GPa [5,8-9].

The laser clad $\text{Ti}_{66}\text{Fe}_{20}\text{Nb}_8\text{Sn}_6$ (at%) alloy coating led to a minimum mean value of 98 GPa (condition LC-3), which is lower than that reported for c.p. Ti and Ti-6Al-4V (126 GPa and 121 GPa, respectively) [17]. Thus, considering both microstructure characteristics and basic properties evaluation, such as hardness and elastic modulus, the laser cladding of $\text{Ti}_{66}\text{Fe}_{20}\text{Nb}_8\text{Sn}_6$ (at%) pre-alloyed powder is able to produce ultrafine composite coatings for implants as a promising route. To the best of our knowledge, it is the first time that combined additions of Sn and Nb are performed for the eutectic Ti-Fe base alloys followed by a comprehensive characterization of the resulting laser cladding coatings into Ti substrate. As a next step, an evaluation of wear properties is desirable for the application perspective of such coatings.

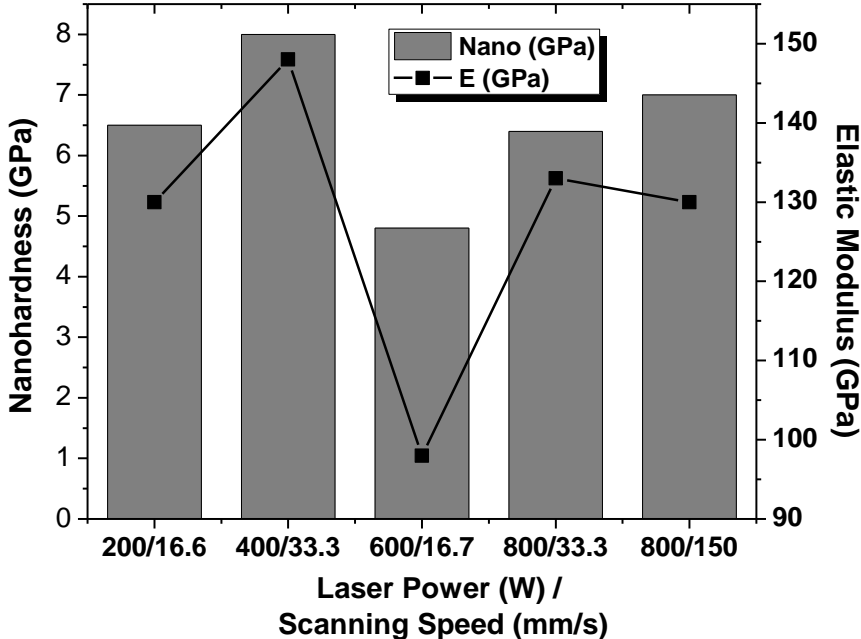


Fig. 14. Variation of Nanohardness (GPa) and Elastic Modulus (GPa) values for coatings produced by laser cladding of $\text{Ti}_{66}\text{Fe}_{20}\text{Nb}_8\text{Sn}_6$ (at%) deposited over a Ti substrate for different combinations of laser parameters: power, P (W) and scanning speed, V_b (mm/s).

4. Conclusions

From the results obtained in this study, the following conclusions can be drawn:

✓ Copper mold cast $\text{Ti}_{66}\text{Fe}_{20}\text{Nb}_8\text{Sn}_6$ (at%) bulk ultrafine nanocomposite alloy in a plate shape ($t = 1$ mm thick) showed a good combination of hard intermetallic TiFe and Ti_3Sn phases finely distributed through a soft β -Ti matrix, resulting in microhardness of 417 HV and low elastic modulus of 72 GPa with suitable properties to be used as implant coatings.

✓ The alloying of pre-placed $\text{Ti}_{66}\text{Fe}_{20}\text{Nb}_8\text{Sn}_6$ (at%) elemental powders, submitted to ball milling, processed through Laser Cladding over a Ti c.p. substrate successfully produced coatings with varied nanohardness (4.8 – 8.0 GPa) and elastic modulus (98 – 150 GPa) depending on laser parameters (power and scanning speed) imposed.

✓ Microstructure and properties of laser clad coatings of Ti-Nb-Fe-Sn alloy can be tuned combining laser power (W) and scanning speeds (mm/s) resulting in varied dilution of alloying elements (coating composition) and stiffness graded coatings for implants. Rapid solidified ultrafine composites were obtained for low laser powers (200W and 400 W) and scanning speeds (16.7mm/s and 33.3 mm/s) and an almost fully β -Ti phase matrix for higher laser powers (600 and 800 W) for more diluted compositions.

✓ The addition of Sn and Fe to the Ti-Nb alloy resulted in ultrafine eutectic composite coatings which lead to high microhardness values. They are strongly related to the volume fraction of the sub-micron dendrites and the nanoscale of the eutectic lamellar spacing of hard TiFe and Ti_3Sn intermetallics interacting with soft β -Ti matrix.

Acknowledgments

The authors acknowledge the financial support provided by CNPq (National Council for Scientific and Technological Development) Universal Project # 473777/2011-8 and FAPESP (São Paulo State Research Foundation) Thematic Project # 2013/05987-8 and Grants # 2015/17090-8 (BEPE of A.L.V.) and # 2015-19978-6 (BPE of C.R.M.A.).

References

- [1] G. He, J. Eckert, W. Löser, L. Schultz, Novel Ti-base nanostructure–dendrite composite with enhanced plasticity, *Nat. Mater.* 2 (2003) 33-37.
- [2] W. Zeiger, M. Schneider, D. Scharnweber, H. Worch, Corrosion behaviour of a nanocrystalline FeAl8 alloy, *Nanostruct. Mater.* 6 (1995) 1013-1016.
- [3] W. Zhang, A. Inoue, High strength Ti–Fe–Sn ultrafine composites with large plasticity, *Scripta Mater.* 57 (2007) 101-104.
- [4] D.K. Misra, S.W. Sohn, H. Gabrisch, W.T. Kim, D.H. Kim, High strength Ti–Fe–(In, Nb) composites with improved plasticity. *Intermetallics*, 18 (2010) 342-347.
- [5] S.A. Souza, C. R. M. Afonso, P.L. Ferrandini, A.A. Coelho, R. Caram, Effect of cooling rate on Ti–Cu eutectoid alloy microstructure, *Mater. Sci. Eng. C*, 29 (2009) 1023-1028.
- [6] J. Das, K.B. Kim, F. Baier, W. Löser, J. Eckert, High-strength Ti-base ultrafine eutectic with enhanced ductility, *Appl. Phys. Lett.* 87 (2005) 161907-1–161907-3.
- [7] D. V. Louzguine-Luzgin, L. V. Louzguina-Luzgina, H. Kato, A. Inoue, Investigation of high strength metastable hypereutectic ternary Ti–Fe–Co and quaternary Ti–Fe–Co–(V, Sn) alloys, *J. Alloys Comp.* 434-435 (2007) 32-35.
- [8] C. R.M. Afonso, P. L. Ferrandini, A. J. R. Londono, R. Caram, High resolution transmission electron microscopy study of the hardening mechanism through phase separation in a β Ti–35Nb–7Zr–5Ta alloy for implant applications, *Acta Biomater.* 6 (2010) 1625-1629.
- [9] F.F. Cardoso, A. Cremasco, R.J. Contieri, E.S.N. Lopes, C.R.M. Afonso, R. Caram, Hexagonal martensite decomposition and phase precipitation in Ti–Cu alloys, *Mater. Design.* 32 (2011) 4608-4613.

- [10] P.N. Andrade, A.A. Coelho, C.R.M. Afonso, R.J. Contieri, MH Robert, R. Caram, Effects of Composition on Solidification Microstructure of Cast Titanium Alloys, *Mater. Sci. Forum.* 649 (2010) 183-188.
- [11] Y.C. Kim, D.H. Bae. W.T. Kim. D.H. Kim, A development of Ti-based bulk metallic glass, *Mater. Sci. Eng. A.* 375-377 (2004) 127-135.
- [12] C.M. Lee, W.F. Ho, C.P. Ju, J.H. Chern Lin, Structure and properties of Titanium-25 Niobium-x Iron alloys, *J. Mater. Sci-Mater. Med.* 13 (2002) 695-700.
- [13] A. O. F. Hayama, P. N. Andrade, A. Cremasco, R. J. Contieri, C. R. M. Afonso, R. Caram, Effects of composition and heat treatment on the mechanical behavior of Ti-Cu alloys, *Mater. Design.* 55 (2014) 1006-1013.
- [14] R.J. Contieri, E.S.N. Lopes, M.T.L. De La Cruz, A.M. Costa, C.R.M. Afonso, R. Caram, Microstructure of Directionally Solidified Ti-Fe Eutectic Alloy with Low Interstitial and High Mechanical Strength, *J. Crystal Growth.* 333 (2011) 40-47.
- [15] J.-J. Oak, D.V. Louzguine-Luzgin. A. Inoue, Fabrication of Ni-free Ti-based bulk-metallic glassy alloy having potential for application as biomaterial, and investigation of its mechanical properties, corrosion, and crystallization behavior, *J. Mater. Res.* 22 (2007) 1346-1353.
- [16] M. A-H.Gepreel, M. Niinomi, Biocompatibility of Ti- alloys for long-term implantation. *J. Mech. Behav. Biomed. Mater.* 20 (2013) 407-415.
- [17] A. Hynowska. E. Pellicer. J. Fornell. S. González. N. van Steenberge. S. Suriñach. A. Gebert. M. Calin. J. Eckert. M.D. Baró. J. Sort, Nanostructured β -phase Ti-31.0Fe-9.0Sn and sub- μ m structured Ti-39.3Nb-13.3Zr-10.7Ta alloys for biomedical applications: Microstructure benefits on the mechanical and corrosion performances, *Mater. Sci. Eng. C.* 32 (2012) 2418-2425
- [18] C. H. Lee. J. T. Kim. S. H. Hong. G. A. Song. J. H. Jo. S. C. Moon. K. B. Kim, Investigation of the Mechanical Properties of Ti-Fe-Sn Ultrafine Eutectic Composites by Dendrite Phase Selection, *Met. Mater. Int.*, 20 (2014) 417-421.
- [19] L. Zhang, H. B. Lu, M. Calin, E. V. Pereloma, J. Eckert, High-strength ultrafine-grained Ti-Fe-Sn alloys with a bimodal structure, *J. Physics: Conf. Series.* 240 (2010) 1-4.
- [20] D.V. Louzguine. H. Kato. L.V. Louzguina. A. Inoue, High-strength binary Ti-Fe bulk alloys with enhanced ductility, *J. Mater. Res.* 19 (2004) 3600-3606.

- [21] G.A. Song, J.H. Han, T.E. Kim, J.M. Park, D.H. Kim, S. Yi, Y. Seo, N.S. Lee, K.B. Kim, Heterogeneous eutectic structure in Ti-Fe-Sn alloys, *Intermetallics* 19 (2011) 536-540.
- [22] A.C. Oliveira, R.H.M. Siqueira, R. Riva, M.S.F. Lima, One-sided laser beam welding of autogenous T-joints for 6013-T4 aluminium alloy, *Mater. Des.* 65 (2015) 726-736.
- [23] J.M. Chaves, O. Florêncio, P.S. Silva, P.W.B. Marques, C.R.M. Afonso, Influence of phase transformations on dynamical elastic modulus and anelasticity of beta Ti-Nb-Fe alloys for biomedical applications, *J. Mech. Beh. Biom. Mater.* 46 (2015) 184-196.
- [24] X.H. Lin, W.L. Johnson, Formation of Ti-Zr-Cu-Ni bulk metallic glasses, *J. Appl. Phys.* 78 (1995) 6514-6519.
- [25] W Kurz and JD Fisher, *Fundamentals of Solidification*, Switzerland: Trans Tech Public; 1992.
- [26] C Brito, G Reinhart, H Nguyen-Thi, N Mangelinck-Noël, N Cheung, J.E. Spinelli, A Garcia, High cooling rate cells, dendrites, microstructural spacings and microhardness in a directionally solidified Al-Mg-Si alloy, *J. Alloys Compd.* 636 (2015) 145-149.
- [27] C.A. Aliravci, M.O. Pekguleryuz, Calculation of phase diagrams for the meta- stable Al-Fe phases forming in direct-chill (DC)-cast aluminum alloy ingots, *Calphad.* 22 (1998) 147-155.
- [28] M.F. Ashby, K.E. Easterling, The transformation hardening of steel surfaces by laser beams-I: hypo-eutectoid steels, *Acta Met.* 32 (1984) 1935-1948.
- [29] P. Gargarella, A. Almeida, R. Vilar, CRM Afonso CRM, S. Peripolli, CT Rios, C Bolfarini, WJ Botta, CS Kiminami, Formation of Fe-based glassy matrix composite coatings by laser processing, *Surf Coat Tech.* 240 (2014) 336-343.
- [30] P. H. Tsai, K. T. Hsu, J. H. Ke, H. C. Lin, J. S. C. Jang & J. C. Huang, Microalloying effect of Si on mechanical properties of Ti based bulk metallic glass, *Materials Technology: Advanced Functional Materials* 30 (2015) 162-166.

List of Figure Captions

Fig. 1. Sequence of processing steps carried out in the Ti-Fe-Nb-Sn alloys: (a) rapid solidification by copper mold in suction casting apparatus followed by a comprehensive microstructural characterization; (b) powder preparation to allow for laser melting to be performed following two conditions, which are: single tracks and overlapped tracks (resultant coatings).

Fig. 2. XRD patterns of $\text{Ti}_{63}\text{Fe}_{23}\text{Nb}_8\text{Sn}_6$ and $\text{Ti}_{66}\text{Fe}_{20}\text{Nb}_8\text{Sn}_6$ (at%) alloys composed mainly of β -Ti matrix and TiFe intermetallic phase ($\text{Ti}_{63}\text{Fe}_{23}\text{Nb}_8\text{Sn}_6$ alloy) and, additionally the Ti_3Sn phase that appears for the $\text{Ti}_{63}\text{Fe}_{23}\text{Nb}_8\text{Sn}_6$ (at%) alloy.

Fig. 3. Typical SEM images obtained for plates with different thickness (t) along the $\text{Ti}_{66}\text{Fe}_{20}\text{Nb}_8\text{Sn}_6$ (at%) alloy casting by suction casting facility.

Fig. 4. Granulometric distribution of the $\text{Ti}_{66}\text{Fe}_{20}\text{Nb}_8\text{Sn}_6$ powder, processed by mechanical milling of elemental powders to be used as pre-placed material for Laser Cladding.

Fig. 5. (a) General and (b) detailed SEM microstructures of the pre-alloyed $\text{Ti}_{66}\text{Fe}_{20}\text{Nb}_8\text{Sn}_6$ powder used in laser process.

Fig. 6. Representative SEM micrographs showing: (a,c,e,g) general shape of the molten pool; (b,d) interface between single Laser affected traces of $\text{Ti}_{66}\text{Fe}_{20}\text{Nb}_8\text{Sn}_6$ (at%) alloy and the surface of the Ti substrate; and (f,h) the growth of dendrites and cells along the laser melted region. $P=200/400\text{W}$; $V_b=16.7/33.3/66.7\text{mm/s}$. \dot{T} is the cooling rate.

Fig. 7. (a), (b) SEM micrographs with features typically found in the interface between laser melted and heat affected zones (HAZ) of the $\text{Ti}_{66}\text{Fe}_{20}\text{Nb}_8\text{Sn}_6$ alloy, and respective X-ray elemental mapping obtained by EDS of (c) Ti-K, (d) Fe-K, (e) Nb-L and (f) Sn-L.

Fig. 8. SEM microstructure of the $\text{Ti}_{66}\text{Fe}_{20}\text{Nb}_8\text{Sn}_6$ alloy emphasizing the presence of fine primary Ti_3Sn dendrites (brighter phases) in the molten pool obtained using the laser process with $P=200\text{W}$ and $V_b=16.7\text{mm/s}$.

Fig. 9. Evolution of Vickers microhardness measured at the cross section of the Laser tracks as a function of power density (PD) for the $\text{Ti}_{66}\text{Fe}_{20}\text{Nb}_8\text{Sn}_6$ alloy.

Fig. 10. XRD patterns of coatings generated from laser cladding of pre-alloyed powders of $\text{Ti}_{66}\text{Fe}_{20}\text{Nb}_8\text{Sn}_6$ alloy for different combinations of laser cladding parameters.

Fig. 11. SEM micrographs of typical coatings profiles obtained by laser cladding of pre-alloyed powders of $\text{Ti}_{66}\text{Fe}_{20}\text{Nb}_8\text{Sn}_6$ alloy for selected combinations of laser parameters: (a)

800W (33.3 mm/s) – LC-1; (b) 600W (16.7 mm/s) – LC-3; (c) 400W (16.7 mm/s) – LC-4; (d) 200W (16.7 mm/s) – LC-5.

Fig. 12. SEM-EBSD results for laser clad coatings of $\text{Ti}_{66}\text{Fe}_{20}\text{Nb}_8\text{Sn}_6$ alloy (condition LC-5) based on (a) IPF-colouring with different orientations and (b) EBSD phase maps. Elemental distributions of (c) iron (Fe) and (d) tin (Sn) along the microstructure regarding the coated zones.

Fig. 13. Graphs showing semi-quantitative compositions through SEM-EDS linescan along the interface between the Ti-Fe-Nb-Sn coating and the Ti substrate processed with power of 600 W and scanning speed of 33.3 mm/s (condition LC-2).

Fig. 14. Variation of Nanohardness (GPa) and Elastic Modulus (GPa) values for coatings produced by laser cladding of $\text{Ti}_{66}\text{Fe}_{20}\text{Nb}_8\text{Sn}_6$ (at%) with basis into a Ti substrate for different combinations of laser parameters: power, P (W) and scanning speed, V_b (mm/s).

List of Table headings

Table 1. Studied alloys and main parameters employed during laser cladding of the Ti-Fe-Nb-Sn alloys.

Table 2. Vickers microhardness ($\text{HV}_{0.2}$) measurements for the ultrafine eutectics of $\text{Ti}_{63}\text{Fe}_{23}\text{Nb}_8\text{Sn}_6$, $\text{Ti}_{60}\text{Fe}_{23}\text{Nb}_8\text{Sn}_9$ and $\text{Ti}_{66}\text{Fe}_{20}\text{Nb}_8\text{Sn}_6$ (at%) alloys.

Table 3. Vickers microhardness values for laser clad tracks and respective coatings with the same combination of laser parameters, power (W) and scanning speed (mm/s) for $\text{Ti}_{66}\text{Fe}_{20}\text{Nb}_8\text{Sn}_6$ (at%) and resulting values of nanohardness and elastic Modulus (GPa).